

Spin reorientation at (110)-La_{2/3}Sr_{1/3}MnO₃/LaCoO₃ interfaces by orbital/charge reconstruction

Cite as: APL Mater. **8**, 021113 (2020); <https://doi.org/10.1063/1.5141005>

Submitted: 02 December 2019 . Accepted: 30 January 2020 . Published Online: 27 February 2020

Furong Han, Xiaobing Chen, Jine Zhang, Jing Zhang, Jinghua Song, Hui Zhang, Hongrui Zhang, Xi Yan, Qinghua Zhang, Lin Gu, Yuansha Chen, Fengxia Hu , Baogen Shen, and Jirong Sun



View Online



Export Citation



CrossMark

ARTICLES YOU MAY BE INTERESTED IN

[Recent progress on the electronic structure, defect, and doping properties of Ga₂O₃](#)

APL Materials **8**, 020906 (2020); <https://doi.org/10.1063/1.5142999>

[Tailoring magnetic order via atomically stacking 3d/5d electrons to achieve high-performance spintronic devices](#)

Applied Physics Reviews **7**, 011401 (2020); <https://doi.org/10.1063/1.5124373>

[Metal oxide catalyzed epitaxy \(MOCATAXY\) of β-Ga₂O₃ films in various orientations grown by plasma-assisted molecular beam epitaxy](#)

APL Materials **8**, 021104 (2020); <https://doi.org/10.1063/1.5135930>

additive manufacturing epitaxial crystal growth cerium oxide polishing powder silver nanoparticles sputtering targets



THE ADVANCED MATERIALS MANUFACTURER®

deposition slugs OLED Lighting spintronics solar energy

osmium nanoribbons thin films chalcogenides AuNPs

GDC li-ion battery electrolytes 99.999% ruthenium spheres

endohedral fullerenes copper nanoparticles diamond micropowder

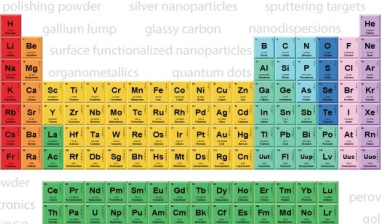
CIGS MBE grade materials palladium catalysts flexible electronics

beta-barium borate borosilicate glass dysprosium pellets YBCO

pyrolytic graphite 3d graphene foam indium tin oxide mesoporous silica

raman substrates sapphire windows tungsten carbide InGaAs

barium fluoride carbon nanotubes lithium niobate scandium powder



gallium lump glassy carbon nanodispersions

surface functionalized nanoparticles organometallics quantum dot

III-IV semiconductors CVD precursors europium phosphors

InAs wafers laser crystals ultra high purity materials MOFs

rare earth metals photovoltaics refractory metals MOCVD

superconductors transparent ceramics ultra high purity silicon

American Elements opens up a world of possibilities so you can **Now Invent!**

Over 15,000 certified high purity laboratory chemicals, metals, & advanced materials and a state-of-the-art Research Center. Printable GHS-compliant Safety Data Sheets. Thousands of new products. And much more. All on a secure multi-language "Mobile Responsive" platform.

perovskite crystals yttrium iron garnet alternative energy h-BN

gold nanocubes graphene oxide macromolecules photonics

rhodium sponge fiber optics beamsplitters infrared dyes zeolites

fused quartz metallocenes platinum ink buckyballs Ti-6Al-4V

Now Invent.™
The Next Generation of Material Science Catalogs

www.americanelements.com



Spin reorientation at (110)-La_{2/3}Sr_{1/3}MnO₃/LaCoO₃ interfaces by orbital/charge reconstruction

Cite as: APL Mater. 8, 021113 (2020); doi: 10.1063/1.5141005

Submitted: 2 December 2019 • Accepted: 30 January 2020 •

Published Online: 27 February 2020



Furong Han,^{1,2} Xiaobing Chen,^{1,2} Jine Zhang,^{1,2} Jing Zhang,^{1,2} Jinghua Song,^{1,2} Hui Zhang,^{1,2} Hongrui Zhang,^{1,2} Xi Yan,^{1,2} Qinghua Zhang,^{1,2} Lin Gu,^{1,2} Yuansha Chen,^{1,2} Fengxia Hu,^{1,2,3}  Baogen Shen,^{1,2,3} and Jirong Sun^{1,2,3,a)}

AFFILIATIONS

¹Beijing National Laboratory for Condensed Matter Physics & Institute of Physics, Chinese Academy of Sciences, Beijing 100190, People's Republic of China

²School of Physical Sciences, University of Chinese Academy of Sciences, Beijing 100049, People's Republic of China

³Songshan Lake Materials Laboratory, Dongguan, Guangdong 523808, People's Republic of China

^{a)}Author to whom correspondence should be addressed: jrsun@iphy.ac.cn

ABSTRACT

The interface reconstruction in perovskite heterostructures caused by interfacial octahedral tilt/rotation and its effects on the spin, charge, and orbital degrees of freedom is a very attractive topic for correlated oxides. Here, we present a systematic investigation on tensely strained (110)-LaCoO₃/La_{2/3}Sr_{1/3}MnO₃/LaCoO₃ trilayers, focusing on orbital reconstruction and accompanied effects. The most remarkable finding is the reordering of the energy levels of Mn-3d orbitals at the interface: the low-lying orbital becomes d_{x²-y²} for sandwiched La_{2/3}Sr_{1/3}MnO₃ rather than d_{3z²-r²} as expected for a bare La_{2/3}Sr_{1/3}MnO₃ film. Interlayer charge transfer via d_{x²-y²} orbitals is further detected as a driving force of orbital reconstruction. Due to spin-orbit coupling, the charge/orbital reconstruction produces a chain effect on the spin degree of freedom of the La_{2/3}Sr_{1/3}MnO₃ layer, resulting in a dramatic spin reorientation by 90° in a film plane. The present work demonstrates how to tune macroscopic properties of correlated oxides via mutual coupling between different degrees of freedom.

© 2020 Author(s). All article content, except where otherwise noted, is licensed under a Creative Commons Attribution (CC BY) license (<http://creativecommons.org/licenses/by/4.0/>). <https://doi.org/10.1063/1.5141005>

INTRODUCTION

Perovskite transition metal oxides (TMOs) with strongly coupled spin, charge, and orbital degrees of freedom provide a valuable playground for the exploration for emergent phenomena.^{1–4} What is of special importance is that the heterostructures are composed of different TMOs, which own unique interface phases with cooperatively distorted oxygen octahedra and reconstructed spin/charge/orbital orders.^{4–10} There are reports on dramatic variations in macroscopic properties for (001) oriented multilayers, produced by even a subtle octahedral tilt/rotation at interfaces.^{11–14} As shown by Liao *et al.*,¹⁵ through transferring the octahedral rotation in NdGaO₃ to the La_{2/3}Sr_{1/3}MnO₃ (LSMO) film, a giant anisotropic transport in ultrathin LSMO films as well as a realignment of the magnetic easy axis can result. In a recent work, Zhang *et al.*¹⁶ demonstrated how symmetry mismatch drove a spin reorientation for the LSMO/LaCoO_{2.5} heterostructures. It was found that, at the

interface, MnO₆ octahedra share the apical oxygen with neighboring CoO₄ tetrahedra, forming elongated octahedra which support perpendicular magnetic anisotropy. The strong effect of the engineered interface was also observed in magnetic oxides other than LSMO. As reported by Kan *et al.*,¹⁷ the SrRuO₃/Ca_{0.5}Sr_{0.5}TiO₃ combination led to a large Ru–O–Ti bond angle; thus, a unique SrRuO₃ phase with a substantially larger Ru–O–Ru bond angle than that of the bulk counterpart is observed.

These works clearly demonstrate the effects of octahedral tilt/rotation on spin ordering. Different from its bulk counterpart, the interface phase suffers from a spatial confinement in the out-of-plane direction. In addition to enhancing quantum fluctuation, this feature will allow a full use of the advantage of interlayer engineering, getting states available for either constituent of the heterostructure.^{18–20} In general, interface engineering takes the effect via modifying the multiple degrees of freedom of the interface phase.^{4,21–23} Due to the strong coupling between different degrees

of freedom, any variation in one degree of freedom will cause a chain effect. Undoubtedly, a deep understanding of the interface effect will strengthen our capabilities to design materials on demand. In this work, we presented a systematic investigation on tensely strained (110)-LCO/LSMO/LCO trilayers (LCO = LaCoO_3), focusing on interface orbital reconstruction and accompanied effects associated with spin degrees of freedom. As reported by Chen *et al.*, the (110)-orientated films exhibit a faster strain relaxation process along the $[1\bar{1}0]$ direction than that along the $[001]$ direction.²⁴ That is to say that the tensile strain along the $[001]$ direction dominates the lattice distortion of the LSMO film deposited on the (110)-STO substrate. This causes the elongation of MnO_6 octahedra along the in-plane $[001]$ axis and the preferred occupation of the $d_{3z^2-r^2}$ orbital.^{25,26} Thus, the magnetic easy-axis of the (110)-LSMO/STO bare film aligns along the $[001]$ axis. In this case, interlayer orbital hybridization and charge transferring are expected to hardly occur due to the absence of the Mn $3d_{3z^2-r^2}$ and O $2p_x$ ($2p_y$) overlap. Surprisingly, we observed a reversion of the energy levels of the $d_{x^2-y^2}$ and $d_{3z^2-r^2}$ orbitals: the low-lying orbital is $d_{x^2-y^2}$ in LSMO of the trilayers. Accompanying orbital reconstruction, a Mn-to-Co charge transfer via the $d_{x^2-y^2}$ orbitals takes place. It is this process that stabilizes the $d_{x^2-y^2}$ orbital. Accordingly, the magnetic easy axis of the LSMO layer undergoes a switching from the $[001]$ to the $[1\bar{1}0]$

direction due to the strong correlation between the orbital and spin degrees of freedom.

METHODS

LCO/LSMO/LCO trilayers [Fig. 1(a)] were grown on (110)- SrTiO_3 (STO) single crystal substrates ($5 \times 3 \times 0.5 \text{ mm}^3$) using the technique of pulsed laser deposition (PLD). During deposition, the temperature of the substrate was maintained at 700°C (for LSMO) or 635°C (for LCO) and the oxygen pressure was fixed to 30 Pa. Here, a low growth temperature was adopted for the LCO layer to avoid recrystallization, which will cause rough interfaces. The repetition rate of the laser pulse was 2 Hz, and the fluence was 2 J/cm^2 (KrF excimer laser, wavelength = 248 nm). After deposition, the samples were cooled to room temperature at the rate of 10°C/min in an oxygen pressure of 100 Pa. The layer thickness was set to 7 nm for LCO and to 4 nm, 5 nm, 9 nm, 10 nm, 15 nm, and 19 nm for LSMO. A (110)-[LCO (3 m)/LSMO (3 m)]₅ ([LCO/LSMO]₅) superlattice sample was also prepared for the measurements of x-ray absorption spectroscopy (XAS), where m means a monolayer and it is $\sim 2.7 \text{ \AA}$. For comparison studies, two bare LSMO films with the thicknesses of 6 nm and 10 nm, respectively, were also fabricated. Here, film thickness has been determined by the number of laser pulses, after a

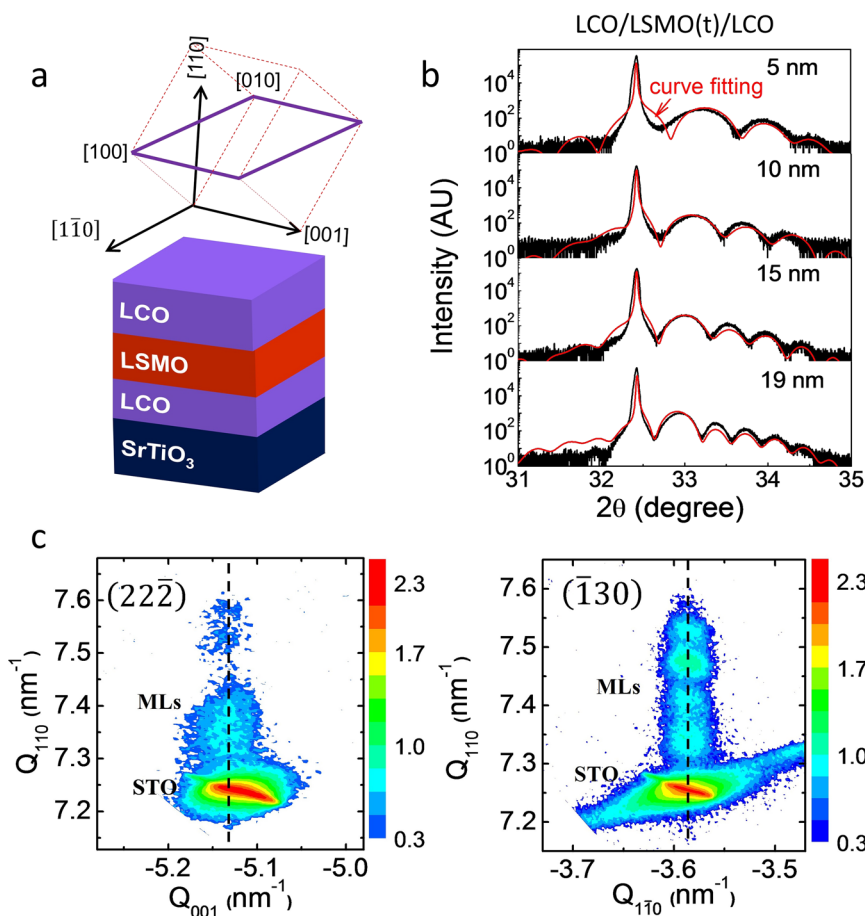


FIG. 1. (a) A sketch for the (110)-LCO/LSMO/LCO trilayers and the relationship between two coordinate systems of $[110]$ - $[1\bar{1}0]$ - $[001]$ and $[001]$ - $[010]$ - $[001]$. (b) XRD spectra of the LCO/LSMO/LCO trilayers with different LSMO thicknesses (black curves). Results of curve-fitting were also represented (red curves). (c) Reciprocal space mapping of the $(22\bar{2})$ (left panel) and $(\bar{1}30)$ (right panel) reflections of the trilayers with $t_{\text{LSMO}} = 10 \text{ nm}$. The vertical alignment of the reflections indicates a fully coherent growth of the trilayers on the substrate, without lattice relaxation. Here, "MLs" denote trilayers. The vertical dashed lines are guides to the eye.

careful calibration by the technique of small angle x-ray reflectivity (Fig. S1 of the [supplementary material](#)).

The surface morphology of the trilayers was measured by using an atomic force microscope (AFM, SPI 3800N, Seiko). The crystal structure of the films was determined by using a Bruker x-ray diffractometer equipped with thin film accessories (D8 Discover, Cu K α radiation). Lattice images were recorded by using a high-resolution scanning transmission electron microscope (STEM) with double C_s correctors (JEOL-ARM200F). Magnetic measurements were conducted by using a quantum-designed vibrating sample magnetometer (VSM-SQUID) in the temperature interval from 5 K to 300 K and the magnetic field range up to 7 T.

The XAS spectra were collected at the Beam line BL08U1A in Shanghai Synchrotron Radiation Facility, in the total electron yield mode. The spectra were measured at the Mn *L*-edge for two polarization directions by setting x-ray polarization to [001] and [1 $\bar{1}$ 0] directions in sequence. The spectra normalization was made by dividing the spectra by a factor such that the *L*₃ pre-edge and *L*₂ post-edge have identical intensities for the two polarizations. After that, the pre-edge spectral region was set to zero and the peak at the *L*₃ edge was set to one. The XLD ($I_{[001]} - I_{[1\bar{1}0]}$) is the intensity difference of normalized XAS along two measurement directions, which gives information on the empty Mn-3*d* states. Co *L*-edge XAS was measured with the x-ray polarization to [001]. The measurement temperature for XAS and XLD is 300 K.

RESULTS AND DISCUSSION

[Figure 1\(a\)](#) is a sketch for the (110)-LCO/LSMO/LCO trilayers and the relationship between two coordinate systems of [110]-[1 $\bar{1}$ 0]-[001] and [001]-[010]-[001]. The trilayers are very smooth, with a root-mean-squared roughness around 0.4 nm (Fig. S2 of the [supplementary material](#)). [Figure 1\(b\)](#) shows the θ -2 θ x-ray diffraction (XRD) spectra for selected LCO/LSMO/LCO trilayers with the LSMO layer thicknesses of $t_{\text{LSMO}} = 5$ nm, 10 nm, 15 nm, and 19 nm. The XRD spectrum is somewhat complex, composed of multiple broad peaks whose number grows with t_{LSMO} . This is the typical feature of trilayers, arising from the diffraction/interference of x-ray between three layers. As shown by the red curve in [Fig. 1\(b\)](#), the calculated curve (red line) mimics the experimental one (black line) very well. Multiple XRD peaks are signatures of high crystal quality of the trilayers. According to the results of curve fitting, the out-of-plane lattice parameter defined by $d_{110} = \sqrt{2}/2a_0$ can be deduced, where a_0 is the lattice parameter of the perovskite unit cell for LSMO or LCO. It is noted that $d_{110} \approx 2.71$ Å for LSMO and ~ 2.68 Å for LCO, smaller than the bulk value (~ 2.74 Å for LSMO and ~ 2.70 Å for LCO). As expected, both films are in-plane tensely strained.

To get the information about the in-plane lattice structure, the reciprocal space mappings (RSMs) of the (22 $\bar{2}$) and (1 $\bar{3}$ 0) reflections are measured. As shown in [Fig. 1\(c\)](#), multiple reflections of the trilayers are also detected by RSMs, aligning vertically with that of the substrate. In addition to a fully coherent growth of the film on the substrate, this result indicates that the trilayers share exactly the same in-plane lattice constant with STO, $a_{001} = 3.905$ Å and $a_{1\bar{1}0} = 5.522$ Å. Therefore, the trilayers are fully tensely strained. This conclusion is consistent with that drawn from curve fitting of the

Θ -2 Θ scanning. Similar results are obtained for other trilayers investigated here (not shown).

[Figure 2\(a\)](#) shows the typical high-angle annular dark-field (HAADF) image of the cross section of (110)-LCO (7 nm)/LSMO (10 nm)/LCO (7 nm), recorded along the [001] zone axis by using a STEM. Here, the brighter and fainter spots correspond to the La/Sr and Mn/Co atomic columns, respectively. Notably, no structural modulation is observed in the bottom LCO layer neighboring substrate (right side LCO). It means that LCO is close to stoichiometric LaCoO₃. In contrast, dark stripes appear in the top LCO layer, indicating the formation of the LaCoO_{3- δ} phase.²⁷⁻²⁹ From first glance, the interface is clear-cut [[Fig. 2\(a\)](#) and the left panel of [Fig. 2\(b\)](#)]. A further analysis of electron energy loss spectroscopy (EELS) shows that the interface is really sharp, with only minor interlayer diffusion to the distance within one unit cell [the right panel of [Fig. 2\(b\)](#)].

To get the information on the orbital structure of the Mn-3*d* electrons, the technique of XAS was adopted. [Figures 3\(a\)](#) and [3\(b\)](#)

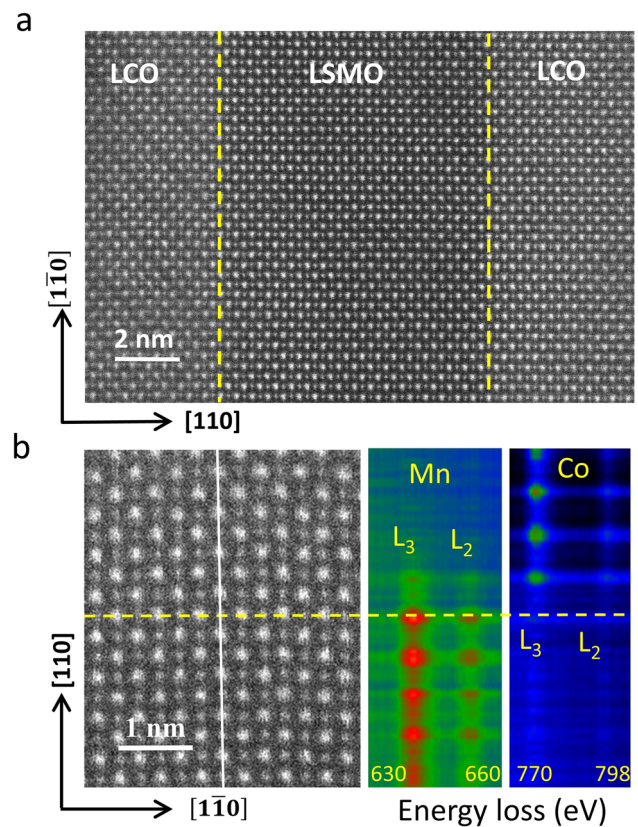


FIG. 2. (a) A typical high-angle annular dark-field (HAADF) image of the cross section of the (110)-LCO/LSMO/LCO trilayers at $t_{\text{LSMO}} = 10$ nm, recorded along the [001] zone axis. Yellow dashed lines mark the LCO/LSMO interfaces. Inclined dark stripes can be observed in the left side LCO layer, which is a typical feature of the oxygen-deficient LCO film. (b) An enlarged view of the HAADF image and the corresponding electron energy loss spectroscopy (EELS) spectrum images of the Mn-*L*_{2,3} and Co-*L*_{2,3} edges, recorded along the white vertical line across the horizontal LSMO/LCO interface. The interface is of high quality, with only minor interlayer diffusion in the range around one unit cell.

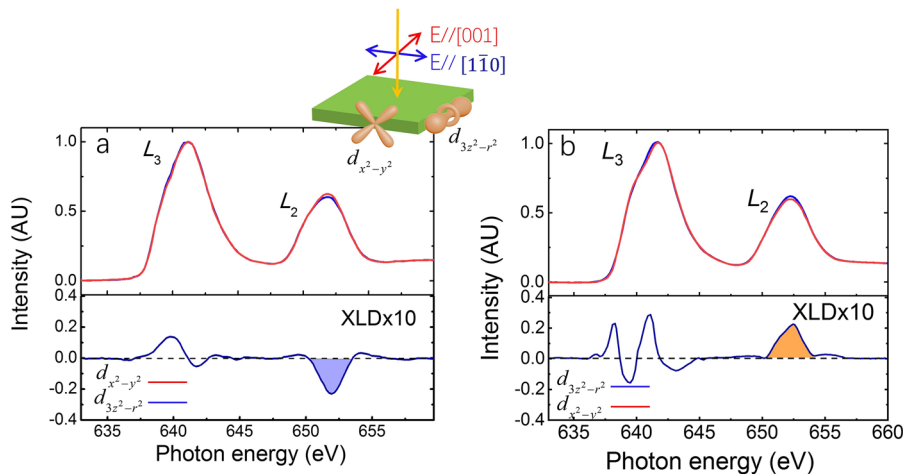


FIG. 3. Normalized Mn-XAS spectra for the bare LSMO film (a) and [LCO (3 m)/LSMO (3 m)]₅ superlattice (b), measured with the optical polarization parallel to the (001) and the (110) planes, respectively. The sketch shows the experiment setup. Bottom panels are the corresponding XLD spectra, amplified by a factor of ten. Shaded areas provide the information on orbital occupancy. The preferentially occupied orbital is $d_{3z^2-r^2}$ for the bare film and $d_{x^2-y^2}$ for superlattices.

show the Mn-XAS spectra of a bare LSMO film (6 nm in thickness) and a [LCO (3 m)/LSMO (3 m)]₅ superlattice, respectively. Here, the superlattice with an ultrathin layer thickness (3 m) was chosen to highlight the interface effect. Since magnetic signals mainly come from the LSMO layer, we only present the Mn- L_2 and L_3 absorption peaks. Two spectra are obtained for each sample by setting x-ray polarization to [001] and [110] directions in sequence.³⁰ As shown by the upper right sketch in Fig. 3(a), [001] and [110] planes are parallel to the $d_{3z^2-r^2}$ and $d_{x^2-y^2}$ orbitals, respectively.^{25,26} Two broad peaks are observed in the interested energy range, corresponding to the L_2 and L_3 absorption edges of Mn 3d electrons.^{31,32} As reported, the L_2 peak contains important information on the orbital structure: a high (low) peak implies a low (high) orbital occupancy.^{8,33} To highlight the difference in the absorption peaks along two directions, x-ray linear dichroism (XLD) spectra, defined by $I_{[001]} - I_{[110]}$, are calculated, where $I_{[001]}$ and $I_{[110]}$ are the peak intensities along the corresponding directions. As well documented, the integration of the XLD spectrum around the L_2 absorption peak gives a direct measure to the occupancy of the $d_{x^2-y^2}$ and $d_{3z^2-r^2}$ orbital states.^{34,35} A negative (positive) value means a preferential occupation of the $d_{3z^2-r^2}$ ($d_{x^2-y^2}$) orbital. For the bare LSMO film, the XLD spectrum exhibits a negative peak around L_2 [the bottom panel of Fig. 3(a)], indicating that the low-lying orbital is $d_{3z^2-r^2}$ when LSMO is in the tensile state. This result is understandable noting that tensile strain will elongate the MnO_6 octahedron along the [001] axis, thus lowering the energy level of $d_{3z^2-r^2}$. Surprisingly, the orbital occupancy is different in the superlattice: the preferred orbital now is $d_{x^2-y^2}$ as implied by the positive XLD peak [Fig. 3(b)] rather than $d_{3z^2-r^2}$ as required by tensile strains. This result is interesting in a sense that it reveals the occurrence of interface coupling-induced orbital reconstruction.

Orbital reconstruction should mainly take place at the LCO/LSMO interfaces since it is invisible when LSMO is thicker than 10 unit cells (not shown). Obviously, interlayer coupling has introduced a mechanism that overcomes the effect of tensile strains, driving $d_{x^2-y^2}$ to a lower energy level than $d_{3z^2-r^2}$. After a careful analysis of the XAS spectra, we found signatures of Mn-to-Co charge transfer. Compared with a bare LSMO layer, the Mn- L_3

(Co- L_3) peak of the superlattices shows a high energy (low energy) shift [Fig. 4(a)]. This result is indicative of an increase (decrease) in the valence state of Mn ions (Co ions).³⁶⁻³⁹ For a (110) film, interlayer charge transfer can only occur between $d_{x^2-y^2}$ orbitals via intermediate O $2p_x$ and $2p_y$ orbitals, which have overlaps with $d_{x^2-y^2}$. This actually implies the establishment of a Mn-O-Co covalent bond.³⁸ It is this bonding process that lowers the energy level of $d_{x^2-y^2}$ [Fig. 4(b)]. Obviously, charge and orbital reconstructions concomitantly take place at interfaces⁷⁻⁹ because of the strong coupling between the corresponding degrees of freedom. As for the $d_{3z^2-r^2}$ orbital, it lies in the film plane and cannot form a chemical bond with the $d_{x^2-y^2}$ or $d_{3z^2-r^2}$ orbital of the neighboring lattice plane. Therefore, it has no contributions to interlayer coupling. From this figure, we can understand the orbital reconstruction in the superlattice. In fact, we have estimated the energy gained by chemical bonding and found that it is ~ 1.5 eV,⁴⁰ i.e., the $d_{x^2-y^2}$ will be considerably lowered by the formation of a covalent bond.

As demonstrated above, by grouping LSMO together with LCO, the orbital/charge structure at the interface is amended. An interesting issue is that how this interface reconstruction affects the spin degree of freedom. Fascinatingly, we found a concomitant spin reorientation: after the orbital/charge reconstruction, spin orientation rotates by 90° in the film plane from the [001] to [110] axis. For a bare LSMO film, as shown in Fig. 5, magnetic moment prefers to align along the [001] direction: The [001] thermomagnetic curve ($M-T$ curve) is well above the [110] one. For trilayers, on the contrary, the [001] curve is always lower than the [110] curve. Similar to trilayers, the easy axis of the superlattices is also along the [110] direction with an even higher anisotropy constant. This is reasonable since superlattices own more interfaces than trilayers (see Fig. S3 of the supplementary material for magnetic data of the superlattice).

A further issue to be addressed is that how the orbital reconstruction modifies the spin orientation. As mentioned above, LSMO owns strongly coupled spin, charge, and orbital degrees of freedom. As well documented, the anisotropy of the spin-orbit energy is directly related to the anisotropy of the orbital moment,^{41,42}

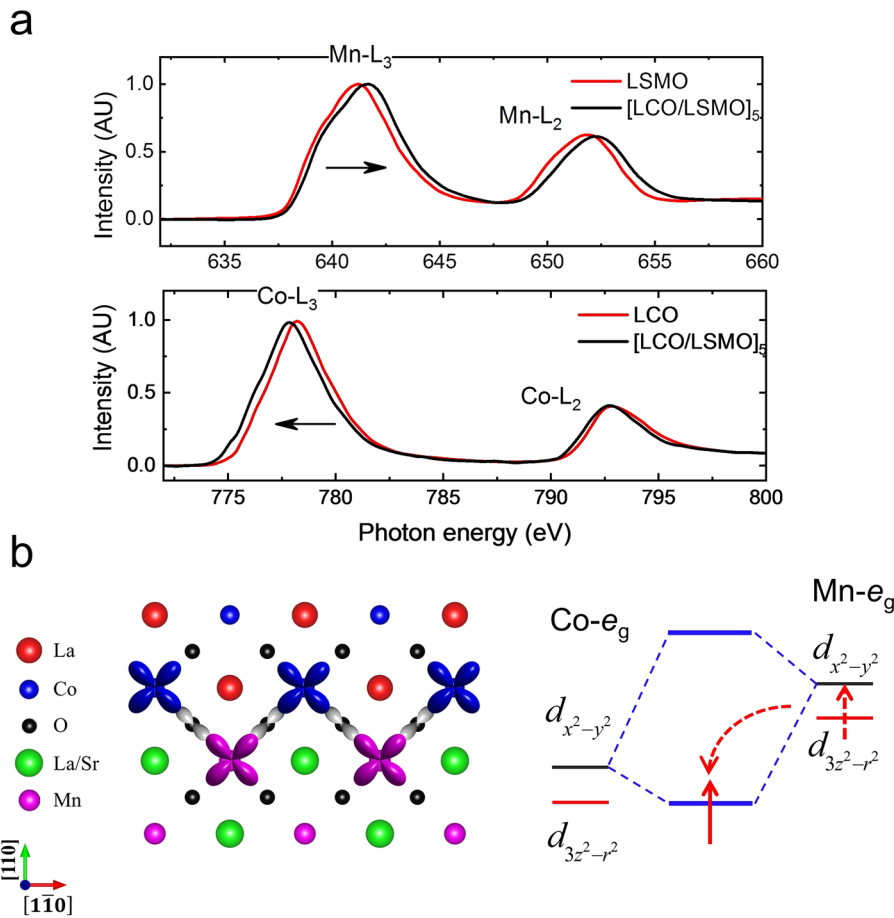


FIG. 4. (a) Normalized Mn- and Co-XAS spectra for the bare LSMO film and [LCO (3 m)/LSMO (3 m)]₅ superlattice. The arrow marks the direction for spectrum shift. (b) Sketch for the overlap of the $d_{x^2-y^2}$ orbitals of Mn-3d and Co-3d electrons, via the O $2p_x$ ($2p_y$) orbital (left panel). It is this overlap that leads to the charge transfer across the LCO/LSMO interface. Due to the formation of the Mn-O-Co covalent bond, the $d_{x^2-y^2}$ orbital is stabilized (right panel). It is possible that the shared electron is closer to Co^{3+} . Consequently, signatures of charge transfer are detected by XAS.

$$\Delta E_{SO} = \zeta \left[\langle \hat{L} \cdot \hat{S} \rangle_{[001]} - \langle \hat{L} \cdot \hat{S} \rangle_{[1\bar{1}0]} \right] = \frac{\zeta}{4\mu_B} (m_o^{[1\bar{1}0]} - m_o^{[001]}), \quad (1)$$

where ζ is a parameter for spin-orbital coupling, m_o is the orbital moment, and $\langle \rangle$ represents a thermodynamic average. For LSMO in trilayers, a direct calculation gives the orbital moment of 0 along the [001] direction and $\frac{1}{2} \left(\frac{3\zeta}{\Delta_{3z^2-r^2, yz}} + \frac{3\zeta}{\Delta_{3z^2-r^2, xz}} \right)$ along the [110]

direction. According to Eq. (1), the easy axis has a larger orbital moment than the hard axis. This means that [110] is the easy axis. For the bare LSMO film, the corresponding values are $\frac{4\zeta}{\Delta_{x^2-y^2, xy}}$ and $\frac{1}{2} \left(\frac{\zeta}{\Delta_{x^2-y^2, yz}} + \frac{\zeta}{\Delta_{x^2-y^2, xz}} \right)$. Accordingly, the easy and hard axes are reversed (see Note 1 of the [supplementary material](#) for detailed calculations).

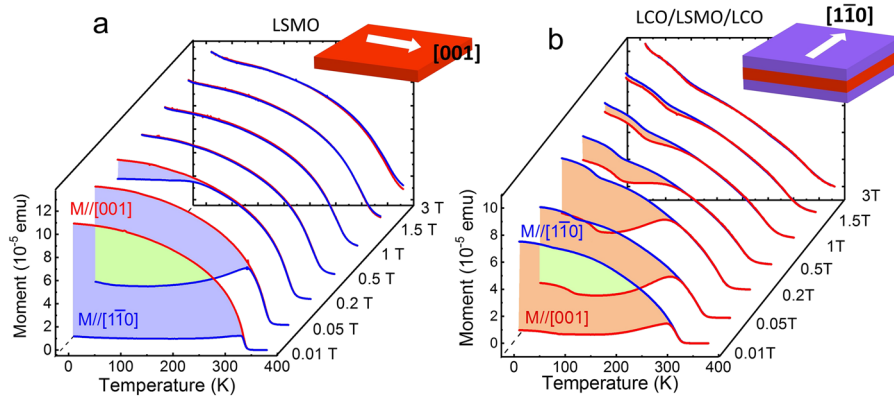


FIG. 5. (a) Thermomagnetic curves of the bare LSMO (10 nm) film, acquired in field-cooling mode with the fields along the [001] and [110] directions, respectively. Shaded areas highlight the magnetic difference along the two measuring directions. Clearly, magnetic moments prefer to align along the [001] direction, as shown by the sketch at the upper right corner. (b) Thermomagnetic curves of the (110) LCO (7 nm)/LSMO (10 nm)/LCO (7 nm) trilayers, measured with exactly the same condition as for the bare LSMO film. The magnetic easy axis at low temperature now is [110].

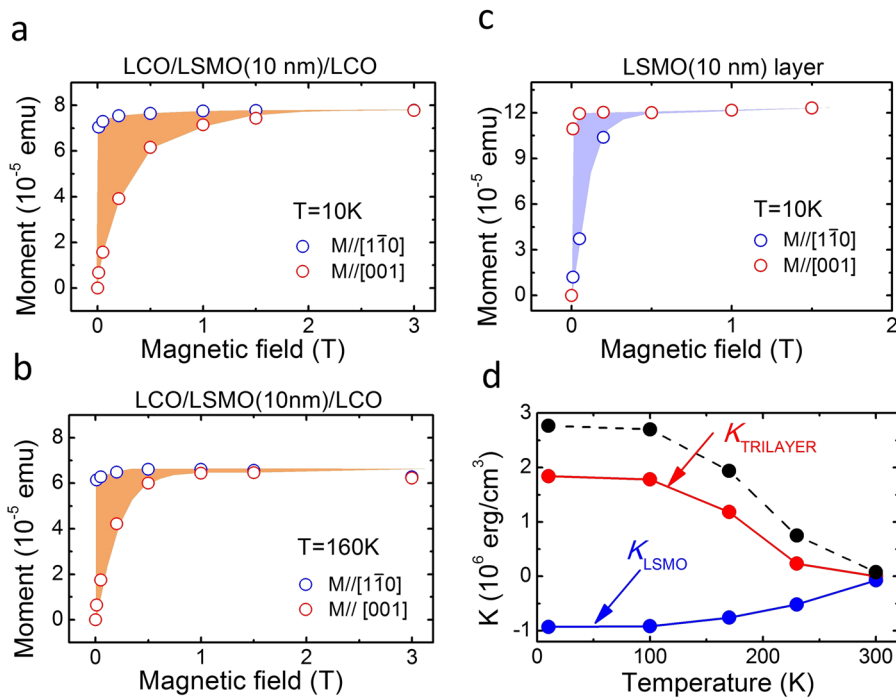


FIG. 6. (a) Magnetic moments as functions of magnetic fields applied along two different directions for the LCO (7 nm)/LSMO (10 nm)/LCO (7 nm) trilayers, obtained at 10 K (a) and 160 K (b). For comparison, the magnetic data of the bare LSMO film are also shown in (c). Shaded area encircled by two M - H curves corresponds to anisotropy energy. (d) Anisotropic constant as a function of temperature. The positive (negative) value indicates a preferred spin direction of $[1\bar{1}0]$ ($[001]$). The dashed line shows the expected anisotropy constants, obtained by subtracting K_{LSMO} from K_{TRILAYER} . Here, the contributions from the LCO layer to K are not considered since the LCO layer is isotropic along the $[001]$ and $[1\bar{1}0]$ directions. Solid lines are a guide to the eye.

To quantitatively describe magnetic anisotropy, we converted the M - T curves in Fig. 5 into a series of M - H curves at different temperatures (see Fig. S4 of the supplementary material for directly measured M - H loops). Figures 6(a) and 6(b) show two typical M - H curves obtained at 10 K and 160 K along different directions. From first glance, the growth rate of M with H is obviously different along the $[1\bar{1}0]$ and $[001]$ directions. Take the data of 10 K as an example. When measured along the $[1\bar{1}0]$ direction, the trilayers get magnetic saturation at very low fields (0.1 T), and further increase in magnetic field only causes minor variation in M . In contrast, along the $[001]$ direction, the saturation state is not gained until the field is above 1.5 T. The energy cost by orientating magnetic moment from easy to hard axes, namely, the anisotropy constant, $K = 1.84 \times 10^6$ erg/cm³ at 10 K, is calculated from the area encircled by the two M - H curves. For the bare LSMO film, however, $K = -0.93 \times 10^6$ erg/cm³ at 10 K. Obviously, the actual anisotropy constant of the trilayers should be larger than that observed here since it has to overcome the intrinsic anisotropy energy of the bare LSMO. A simple calculation yields $\Delta K = 2.77 \times 10^6$ erg/cm³ for trilayers. This value is larger by a factor of three in magnitude than that of the bare LSMO layer. Obviously, the effect of interface reconstruction is much stronger than the strain effect.

Based on Eq. (1), we can get an estimation of anisotropic energy. For LSMO, Mn possesses a spin-orbital coupling coefficient of $\zeta = 0.045$ eV⁴³ and an orbital magnetic moment of $\sim 0.1 \mu_B$.⁴⁴ Based on the density functional theory calculations, the orbital magnetic moment difference along two orthogonal directions can be up to $\Delta\mu_L = 0.01 \mu_B$.⁴⁵ Adopting this $\Delta\mu_L$, the calculated anisotropy constant is $\sim 10^6$ erg/cm³, which is consistent with the experimental value obtained for our LCO/LSMO heterostructure.

Following a similar procedure, the anisotropy constant at high temperatures can be obtained. As shown in Fig. 6(d), K is maximal at low temperatures, nearly constant from 10 K to 100 K, and rapidly decreases upon further warming up above 100 K. The decrease in K with temperature can be ascribed to the decrease in the magnetization of the LSMO layer.

If the anomalous magnetic anisotropy stems from interface reconstruction, it should be dependent on the layer thickness of LSMO (t_{LSMO}). In Figs. 7(a)–7(c), we show the isothermal magnetization curves of the trilayers with different LSMO layers (see Fig. S5 of the supplementary material for M - T curves measured under different applied fields). From first glance, the discrepancy of the two M - H curves along two directions reduces as layer thickness grows. This feature is especially obvious as t_{LSMO} increases from 10 nm to 19 nm. It implies a reduction in anisotropy energy. A direct calculation shows that K is $\sim 2.55 \times 10^6$ erg/cm³ for $t_{\text{LSMO}} = 5$ nm and $\sim 0.6 \times 10^6$ erg/cm³ for $t_{\text{LSMO}} = 19$ nm. The maximal anisotropy constant is 5.8×10^6 erg/cm³, gained in the $[\text{LCO}(3\text{ m})/\text{LSMO}(3\text{ m})]_5$ superlattice. Figure 7(d) shows the anisotropy constant as a function of the reciprocal layer thickness of LSMO. Although the K - $1/t_{\text{LSMO}}$ relation is nonlinear, K displays a clear tendency toward growth as t_{LSMO} decreases. This result confirms the dominative role of the interface effect.⁴⁶

Finally, we emphasize that the effect of interface reconstruction on spin orientation is strong only for tensile trilayers. For compressive trilayers, charge transfer takes place via both $d_{3z^2-r^2}$ and $d_{x^2-y^2}$ orbitals. In this case, which orbital is more stable depends on the competition of these two orbitals. Consequently, the interface effect on the spin degree of freedom could be weakened. To investigate the effect of interface coupling in the

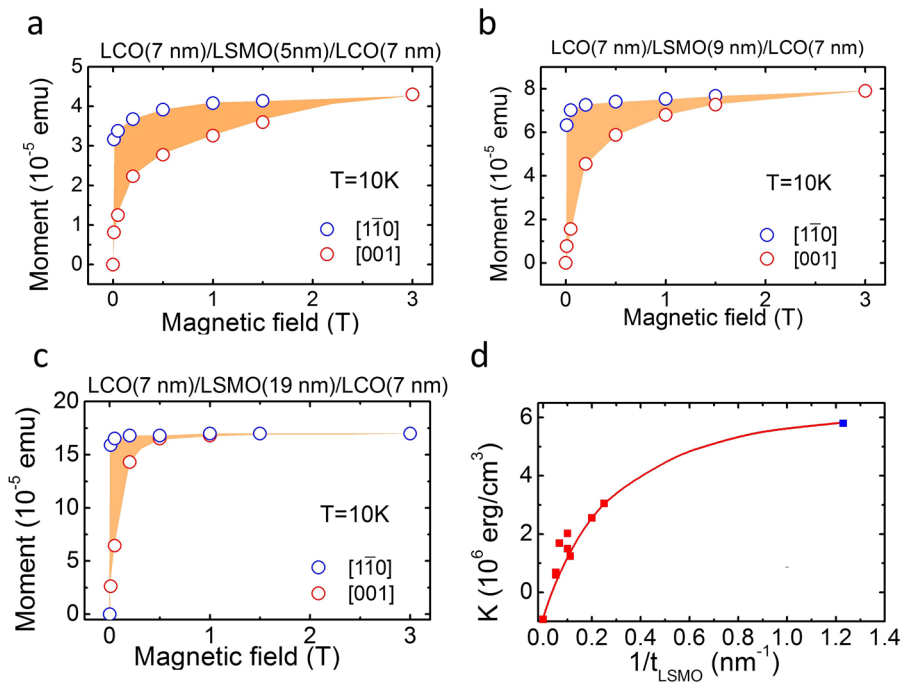


FIG. 7. Isothermal magnetization curves measured at 10 K along the [110] and [001] directions, respectively, for selected samples with different thicknesses of the LSMO layer. The LSMO layer thickness is 5 nm (a), 9 nm (b), and 19 nm (c). (d) Anisotropy constant as a function of layer thickness of LSMO. The last data point in this curve comes from the superlattice. The solid line is a guide to the eye.

compressive state, we choose the combination of $\text{La}_{2/3}\text{Ba}_{1/3}\text{MnO}_3$ (LBMO) and $(\text{LaAlO}_3)_{0.3}(\text{SrAl}_{0.5}\text{Ta}_{0.5}\text{O}_3)_{0.7}$ (LSAT) substrates (the lattice constant is 3.91 Å for LBMO and 3.86 Å for LSAT). The compressive strain of the LBMO/LSAT film is about -1%, which is exactly opposite to that of the LSMO/STO film (tensile 1%). We have fabricated compressive trilayers LCO/LBMO/LCO on the LSAT substrate. As expected, the preferred spin orientation is [110]. The interface effect only enhanced anisotropy energy by $\Delta K = 2.2 \times 10^5 \text{ erg/cm}^3$ (see Fig. S6 of the [supplementary material](#)) for $\text{La}_{2/3}\text{Ba}_{1/3}\text{MnO}_3$ ($T = 100 \text{ K}$), while it causes an increment of $\Delta K = 2.7 \times 10^6 \text{ erg/cm}^3$ for tensile LCO/LSMO/LCO at 100 K [Fig. 6(d)].

CONCLUSIONS

In conclusion, a systematic investigation on tensely strained (110)- $\text{LaCoO}_3/\text{La}_{2/3}\text{Sr}_{1/3}\text{MnO}_3/\text{LaCoO}_3$ trilayers is presented, focusing on the orbital reconstruction at interfaces and the effect stemming from spin-orbital coupling. It is found that the interlayer coupling makes Mn $3d_{x^2-y^2}$ preferentially occupied, overcoming the effect of tensile strains which stabilizes $d_{3z^2-r^2}$. We present evidences for interlayer charge transfer via $d_{x^2-y^2}$ orbitals. This causes the formation of Mn-O-Co covalence, thus lowering the energy level of $d_{x^2-y^2}$. In response to orbital reconstruction, the spin orientation of $\text{La}_{2/3}\text{Sr}_{1/3}\text{MnO}_3$ undergoes a 90° switching in the film plane due to spin, charge, and orbital coupling. This work demonstrates how spin, charge, and orbital degrees of freedom couple with each other during the interface reconstruction, paving the way toward the exploration for novel materials.

SUPPLEMENTARY MATERIAL

See the [supplementary material](#) for the schematic representation of the x-ray reflectivity, surface morphology, thermomagnetic curves, and magnetic hysteresis loop of the LCO/LSMO/LCO trilayers; thermomagnetic curves and magnetic hysteresis loop of the [LCO/LSMO]₅ superlattice, LCO/LBMO/LCO trilayers, and bare LBMO; and the detailed calculations of orbital momentum.

AUTHOR'S CONTRIBUTIONS

F.H. and X.C. contributed equally to this work.

ACKNOWLEDGMENTS

This work has been supported by the National Basic Research of China (Grant Nos. 2016YFA0300701, 2018YFA0305704, and 2017YFA0206300), the National Natural Science Foundation of China (Grant Nos. 11934016, 11520101002, 11574006, 51590880, 51531008, and 11604265), the Project for Innovative Research Team of the National Natural Science Foundation of China (Grant Nos. 11921004), and the Key Program of the Chinese Academy of Sciences. We acknowledge Beamline BL08U1A in Shanghai Synchrotron Radiation Facility (SSRF) for the XAS and XLD measurements.

There are no conflicts of interest to declare.

REFERENCES

- M. B. Salamon and M. Jaime, "The physics of manganites: Structure and transport," *Rev. Mod. Phys.* **73**, 583–628 (2001).
- Y. Tokura and N. Nagaosa, "Orbital physics in transition-metal oxides," *Science* **288**, 462–468 (2000).

- ³E. Dagotto, "Complexity in strongly correlated electronic systems," *Science* **309**, 257–262 (2005).
- ⁴H. Y. Hwang, Y. Iwasa, M. Kawasaki, B. Keimer, N. Nagaosa, and Y. Tokura, "Emergent phenomena at oxide interfaces," *Nat. Mater.* **11**, 103–113 (2012).
- ⁵X. Zhai, L. Cheng, Y. Liu, C. M. Schlepueetz, S. Dong, H. Li, X. Zhang, S. Chu, L. Zheng, J. Zhang *et al.*, "Correlating interfacial octahedral rotations with magnetism in $(\text{LaMnO}_{3+\delta})\text{(N)}/(\text{SrTiO}_3)\text{(N)}$ superlattices," *Nat. Commun.* **5**, 4283 (2014).
- ⁶J. M. Rondinelli, S. J. May, and J. W. Freeland, "Control of octahedral connectivity in perovskite oxide heterostructures: An emerging route to multifunctional materials discovery," *MRS Bull.* **37**, 261–270 (2012).
- ⁷J. Chakhalian, J. W. Freeland, H. U. Habermeier, G. Cristiani, G. Khaliullin, M. van Veenendaal, and B. Keimer, "Orbital reconstruction and covalent bonding at an oxide interface," *Science* **318**, 1114–1117 (2007).
- ⁸B. Cui, C. Song, F. Li, G. Y. Wang, H. J. Mao, J. J. Peng, F. Zeng, and F. Pan, "Tuning the entanglement between orbital reconstruction and charge transfer at a film surface," *Sci. Rep.* **4**, 4206 (2014).
- ⁹J. Garcia-Barriocanal, J. C. Cezar, F. Y. Bruno, P. Thakur, N. B. Brookes, C. Urfeld, A. Rivera-Calzada, S. R. Giblin, J. W. Taylor, J. A. Duffy *et al.*, "Spin and orbital Ti magnetism at $\text{LaMnO}_3/\text{SrTiO}_3$ interfaces," *Nat. Commun.* **1**, 82 (2010).
- ¹⁰S. Okamoto and A. J. Millis, "Electronic reconstruction at an interface between a Mott insulator and a band insulator," *Nature* **428**, 630–633 (2004).
- ¹¹J. He, A. Borisevich, S. V. Kalinin, S. J. Pennycook, and S. T. Pantelides, "Control of octahedral tilts and magnetic properties of perovskite oxide heterostructures by substrate symmetry," *Phys. Rev. Lett.* **105**, 227203 (2010).
- ¹²A. Y. Borisevich, H. J. Chang, M. Huijben, M. P. Oxley, S. Okamoto, M. K. Niranjana, J. D. Burton, E. Y. Tsybaly, Y. H. Chu, P. Yu *et al.*, "Suppression of octahedral tilts and associated changes in electronic properties at epitaxial oxide heterostructure interfaces," *Phys. Rev. Lett.* **105**, 087204 (2010).
- ¹³R. Aso, D. Kan, Y. Shimakawa, and H. Kurata, "Atomic level observation of octahedral distortions at the perovskite oxide heterointerface," *Sci. Rep.* **3**, 2214 (2013).
- ¹⁴D. Yi, C. L. Flint, P. P. Balakrishnan, K. Mahalingam, B. Urwin, A. Vailionis, A. T. N'Diaye, P. Shafer, E. Arenholz, Y. Choi *et al.*, "Tuning perpendicular magnetic anisotropy by oxygen octahedral rotations in $(\text{La}_{1-x}\text{Sr}_x\text{MnO}_3)/(\text{SrIrO}_3)$ superlattices," *Phys. Rev. Lett.* **119**, 077201 (2017).
- ¹⁵Z. Liao, M. Huijben, Z. Zhong, N. Gauquelin, S. Macke, R. J. Green, S. Van Aert, J. Verbeeck, G. Van Tendeloo, K. Held *et al.*, "Controlled lateral anisotropy in correlated manganite heterostructures by interface-engineered oxygen octahedral coupling," *Nat. Mater.* **15**, 425–431 (2016).
- ¹⁶J. Zhang, Z. Zhong, X. Guan, X. Shen, J. Zhang, F. Han, H. Zhang, H. Zhang, X. Yan, Q. Zhang *et al.*, "Symmetry mismatch-driven perpendicular magnetic anisotropy for perovskite/brownmillerite heterostructures," *Nat. Commun.* **9**, 1923 (2018).
- ¹⁷D. Kan, R. Aso, R. Sato, M. Haruta, H. Kurata, and Y. Shimakawa, "Tuning magnetic anisotropy by interfacially engineering the oxygen coordination environment in a transition metal oxide," *Nat. Mater.* **15**, 432–437 (2016).
- ¹⁸A. Ohtomo and H. Y. Hwang, "A high-mobility electron gas at the $\text{LaAlO}_3/\text{SrTiO}_3$ heterointerface," *Nature* **427**, 423–426 (2004).
- ¹⁹N. Reyren, S. Thiel, A. D. Caviglia, L. F. Kourkoutis, G. Hammerl, C. Richter, C. W. Schneider, T. Kopp, A. S. Ruetschi, D. Jaccard *et al.*, "Superconducting interfaces between insulating oxides," *Science* **317**, 1196–1199 (2007).
- ²⁰A. Brinkman, M. Huijben, M. Van Zalk, J. Huijben, U. Zeitler, J. C. Maan, W. G. Van der Wiel, G. Rijnders, D. H. A. Blank, and H. Hilgenkamp, "Magnetic effects at the interface between non-magnetic oxides," *Nat. Mater.* **6**, 493–496 (2007).
- ²¹P. Zubko, S. Gariglio, M. Gabay, P. Ghosez, and J.-M. Triscone, "Interface physics in complex oxide heterostructures," *Annu. Rev. Condens. Matter Phys.* **2**, 141–165 (2011).
- ²²H. Yamada, Y. Ogawa, Y. Ishii, H. Sato, M. Kawasaki, H. Akoh, and Y. Tokura, "Engineered interface of magnetic oxides," *Science* **305**, 646–648 (2004).
- ²³J. D. Hoffman, B. J. Kirby, J. Kwon, G. Fabbri, D. Meyers, J. W. Freeland, I. Martin, O. G. Heinonen, P. Steadman, H. Zhou *et al.*, "Oscillatory noncollinear magnetism induced by interfacial charge transfer in superlattices composed of metallic oxides," *Phys. Rev. X* **6**, 041038 (2016).
- ²⁴Y. Z. Chen, J. R. Sun, S. Liang, W. M. Lv, B. G. Shen, and W. B. Wu, "Effect of anisotropic strain on the charge ordering transition in manganite films," *J. Appl. Phys.* **103**, 096105 (2008).
- ²⁵D. Pesquera, G. Herranz, A. Barla, E. Pellegrin, F. Bondino, E. Magnano, F. Sanchez, and J. Fontcuberta, "Surface symmetry-breaking and strain effects on orbital occupancy in transition metal perovskite epitaxial films," *Nat. Commun.* **3**, 1189 (2012).
- ²⁶Z. Quan, B. Wu, F. Zhang, G. Zhou, J. Zang, and X. Xu, "Room temperature insulating ferromagnetism induced by charge transfer in ultrathin $\text{La}_{0.7}\text{Sr}_{0.3}\text{MnO}_3$ films," *Appl. Phys. Lett.* **110**, 072405 (2017).
- ²⁷Y.-M. Kim, J. He, M. D. Biegalski, H. Ambaye, V. Lauter, H. M. Christen, S. T. Pantelides, S. J. Pennycook, S. V. Kalinin, and A. Y. Borisevich, "Probing oxygen vacancy concentration and homogeneity in solid-oxide fuel-cell cathode materials on the subunit-cell level," *Nat. Mater.* **11**, 888–894 (2012).
- ²⁸M. T. Anderson, J. T. Vaughey, and K. R. Poeppelmeier, "Structural similarities among oxygen-deficient perovskites," *Chem. Mater.* **5**, 151–165 (1993).
- ²⁹H. Jeon, W. S. Choi, J. W. Freeland, H. Ohta, C. U. Jung, and H. N. Lee, "Topotactic phase transformation of the Brownmillerite $\text{SrCoO}_{2.5}$ to the perovskite $\text{SrCoO}_{3-\delta}$," *Adv. Mater.* **25**, 3651–3656 (2013).
- ³⁰J. Heidler, C. Piamonteze, R. V. Chopdekar, M. A. Uribe-Laverde, A. Alberca, M. Buzzi, A. Uldry, B. Delley, C. Bernhard, and F. Nolting, "Manipulating magnetism in $\text{La}_{0.7}\text{Sr}_{0.3}\text{MnO}_3$ via piezostain," *Phys. Rev. B* **91**, 024406 (2015).
- ³¹D. J. Huang, W. B. Wu, G. Y. Guo, H. J. Lin, T. Y. Hou, C. F. Chang, C. T. Chen, A. Fujimori, T. Kimura, H. B. Huang *et al.*, "Orbital ordering in $\text{La}_{0.5}\text{Sr}_{1.5}\text{MnO}_4$ studied by soft x-ray linear dichroism," *Phys. Rev. Lett.* **92**, 087202 (2004).
- ³²D. J. Huang, W. B. Wu, G. Y. Guo, H. J. Lin, T. Y. Hou, C. F. Chang, C. T. Chen, A. Fujimori, T. Kimura, H. B. Huang *et al.*, "Strong linear dichroism in $\text{Mn L}_{2,3}$ -L₃ absorption predicted for orbital ordering in LaMnO_3 ," *J. Phys. Soc. Jpn.* **69**, 2399–2402 (2000).
- ³³M. Huijben, L. W. Martin, Y. H. Chu, M. B. Holcomb, P. Yu, G. Rijnders, D. H. A. Blank, and R. Ramesh, "Critical thickness and orbital ordering in ultrathin $\text{La}_{0.7}\text{Sr}_{0.3}\text{MnO}_3$ films," *Phys. Rev. B* **78**, 094413 (2008).
- ³⁴A. Tebano, C. Aruta, S. Sanna, P. G. Medaglia, G. Balestrino, A. A. Sidorenko, R. De Renzi, G. Ghiringhelli, L. Braicovich, V. Bisogni *et al.*, "Evidence of orbital reconstruction at interfaces in ultrathin $\text{La}_{0.67}\text{Sr}_{0.33}\text{MnO}_3$ films," *Phys. Rev. Lett.* **100**, 137401 (2008).
- ³⁵C. Aruta, G. Ghiringhelli, A. Tebano, N. G. Boggio, N. B. Brookes, P. G. Medaglia, and G. Balestrino, "Strain induced x-ray absorption linear dichroism in $\text{La}_{0.7}\text{Sr}_{0.3}\text{MnO}_3$ thin films," *Phys. Rev. B* **73**, 235121 (2006).
- ³⁶L. Wu, M. Chen, C. Li, J. Zhou, L. Shen, Y. Wang, Z. Zhong, M. Feng, Y. Zhang, K. Han *et al.*, "Ferromagnetism and matrix-dependent charge transfer in strained LaMnO_3 - LaCoO_3 superlattices," *Mater. Res. Lett.* **6**, 501–507 (2018).
- ³⁷J. Peng, C. Song, F. Li, B. Cui, H. Mao, Y. Wang, G. Wang, and F. Pan, "Charge transfer and orbital reconstruction in strain-engineered $(\text{La,Sr})\text{MnO}_3/\text{LaNiO}_3$ heterostructures," *ACS Appl. Mater. Interfaces* **7**, 17700–17706 (2015).
- ³⁸B. Cui, F. Li, C. Song, J. J. Peng, M. S. Saleem, Y. D. Gu, S. N. Li, K. L. Wang, and F. Pan, "Insight into the antiferromagnetic structure manipulated by electronic reconstruction," *Phys. Rev. B* **94**, 134403 (2016).
- ³⁹H. Jeon, W. S. Choi, M. D. Biegalski, C. M. Folkman, I. C. Tung, D. D. Fong, J. W. Freeland, D. Shin, H. Ohta, M. F. Chisholm *et al.*, "Reversible redox reactions in an epitaxially stabilized SrCoO_x oxygen sponge," *Nat. Mater.* **12**, 1057–1063 (2013).
- ⁴⁰P. Mahadevan, N. Shanthi, and D. D. Sarma, "Estimates of electronic interaction parameters for LaMO_3 compounds (M=Ti-Ni) from ab initio approaches," *Phys. Rev. B* **54**, 11199–11206 (1996).
- ⁴¹P. Bruno, "Tight-Binding approach to the orbital magnetic-moment and magnetocrystalline anisotropy of transition-metal monolayers," *Phys. Rev. B* **39**, 865–868 (1989).
- ⁴²P. Bruno, *Magnetismus Von Festkörpern und Grenzflächen* (KFA, Jülich, Germany, 1993), Chap. 24, p. 1.
- ⁴³E. Francisco and L. Pueyo, "Accurate calculation of spin-orbit coupling constants for 3d atoms and ions with effective core potentials and reduced basis sets," *Phys. Rev. A* **36**, 1978 (1987).

⁴⁴T. Koide, H. Miyauchi, J. Okamoto, T. Shidara, T. Sekine, T. Saitoh, A. Fujimori, H. Fukutani, M. Takano, and Y. Takeda, "Close correlation between the magnetic moments, lattice distortions, and hybridization in LaMnO_3 and $\text{La}_{1-x}\text{Sr}_x\text{MnO}_{3+\delta}$: Doping-dependent magnetic circular x-ray dichroism study," *Phys. Rev. Lett.* **87**, 246404 (2001).

⁴⁵D. Odkhuu and N. Kioussis, "Strain-driven electric control of magnetization reversal at multiferroic interfaces," *Phys. Rev. B* **97**, 094404 (2018).

⁴⁶M. T. Johnson, P. J. H. Bloemen, F. J. A. denBroeder, and J. J. deVries, "Magnetic anisotropy in metallic multilayers," *Rep. Prog. Phys.* **59**, 1409–1458 (1996).